ARTICLE OPEN

Check for updates

Giant Dzyaloshinskii-Moriya interaction, strong XXZ-type biquadratic coupling, and bimeronic excitations in the two-dimensional $CrMnI_6$ magnet

Shunhong Zhang[1], Xiaoyin Li[1], Huisheng Zhang[2], Ping Cui[1,3], Xiaohong Xu[2] and Zhenyu Zhang[1,3]✉

Two-dimensional magnets have been discovered recently as a new class of quantum matter exhibiting a broad wealth of exotic phenomena, including notably various topological excitations rooted in emergent exchange couplings between the localized magnetic moments. By analyzing the anisotropies in the single-ion magnetization and two-body exchange couplings obtained from first-principles calculations, we reveal coexistence of both giant Dzyaloshinskii–Moriya interaction and strong anisotropic XXZ-type biquadratic coupling in a recently predicted monolayer $CrMnI_6$ magnet. The former is induced by the spontaneous in-plane inversion symmetry breaking in the bipartite system, the latter is inherently tied to the distinct high-spin state of the Mn sublattice, while the large magnitudes of both stem from the significant spin-orbit coupling. Next, we use atomistic magnetics simulations to demonstrate the vital role of Dzyaloshinskii–Moriya interaction in harboring topological bimeronic excitations, and show that the biquadratic coupling favors a Berezinskii–Kosterlitz–Thouless-like transition as the system reduces its temperature from the paramagnetic phase. These findings substantially enrich our understanding of the microscopic couplings in 2D magnets, with appealing application potentials.

npj Quantum Materials (2023)8:38 ; https://doi.org/10.1038/s41535-023-00569-4

INTRODUCTION

It has long been recognized that dimensionality plays an essential role in magnetic systems and can drastically influence their ordering behavior, low-energy excitations, and magneto-transport properties, due to delicate interplays of the different microscopic couplings between localized moments. In particular, studies of magnetism in two-dimensional (2D) systems within the regime of isotropic coupling have led to major conceptual advances including the Hohenberg–Mermin–Wanger theorem[1,2] and Berezinskii–Kosterlitz–Thouless transition[3–5]. The former stipulates that Landau-type magnetic ordering is absent in rotationally invariant 2D systems, while the latter is manifested by distinctly new topological characteristics as the systems reduce their temperatures from the paramagnetic phase. Recent breakthrough advances in 2D ferromagnets of CrI_3 and $CrGeTe_3$, however, have unambiguously shown that the Hohenberg–Mermin–Wanger restriction can be lifted, thanks to sufficiently strong anisotropy in the exchange couplings[6,7]. These developments offer compelling opportunities for exploration of a broad wealth of exotic phenomena.

Anisotropic magnetic interactions can exist in various forms, but in essence are all rooted in spin-orbit coupling of electrons. Such anisotropies can be further classified into onsite and multi-site terms. The simplest onsite anisotropy is originated from the atomic-scale spin-orbit coupling that breaks the spatial rotational symmetry, favoring magnetization along a particular direction. Among the multi-site anisotropies, the celebrated example is the Dzyaloshinskii–Moriya interaction (DMI)[8,9], favoring perpendicular mutual alignment between two localized moments. Past studies have shown that the DMI is essential in enabling the formation of various chiral or topological entities in magnetic systems, including chiral domain walls[10], skyrmions[11–13], and merons[14]. Yet given their inherent inversion symmetry, the DMI is largely absent in pristine monolayer CrI_3 and $CrGeTe_3$ at least at the nearest neighboring level[15,16], and additional manipulations or materials modifications have to be invoked to break the inversion symmetry of such 2D magnets in order to induce significant DMI[17–21].

In this paper, we use first-principles calculations to analyze the onsite and inter-site exchange anisotropies in a recently predicted monolayer magnet of $CrMnI_6$, and reveal the striking coexistence of both giant DMI and strong XXZ-type biquadratic coupling. Qualitatively, the DMI is induced by the spontaneous in-plane inversion symmetry breaking in the bipartite system, which distinctly contrasts all the schemes to induce DMI via out-of-plane inversion symmetry breakings reported so far[17–21], while the exotic XXZ-type biquadratic coupling is inherently tied to the high-spin state of the Mn sublattice. At a quantitative level, the large magnitudes of both anisotropic terms stem from the significant spin-orbit coupling within the system. Next, we use atomistic magnetics simulations to demonstrate the vital role of DMI in harboring topological bimeronic excitations, while the biquadratic coupling favors a Berezinskii–Kosterlitz–Thouless-like transition as the system reduces its temperature from the paramagnetic phase. These findings substantially enrich our understanding of the microscopic couplings in 2D magnets, which can be further exploited for various technological applications in memory devices.

RESULTS

Giant DMI in the bipartite $CrMnI_6$ monolayer

We first contrast two distinctive means of breaking inversion symmetry between two magnetic sites for inducing DMI. The scheme illustrated in Fig. 1a, which has been extensively

[1]International Center for Quantum Design of Functional Materials (ICQD), University of Science and Technology of China, 96 Jinzhai Road, Hefei 230026 Anhui, China. [2]Key Laboratory of Magnetic Molecules and Magnetic Information Materials of the Ministry of Education and Research Institute of Materials Science, Shanxi Normal University, No. 339, Taiyu Road, Taiyuan 030000 Shanxi, China. [3]Hefei National Laboratory, University of Science and Technology of China, Hefei 230088, Anhui, China. ✉email: zhangzy@ustc.edu.cn

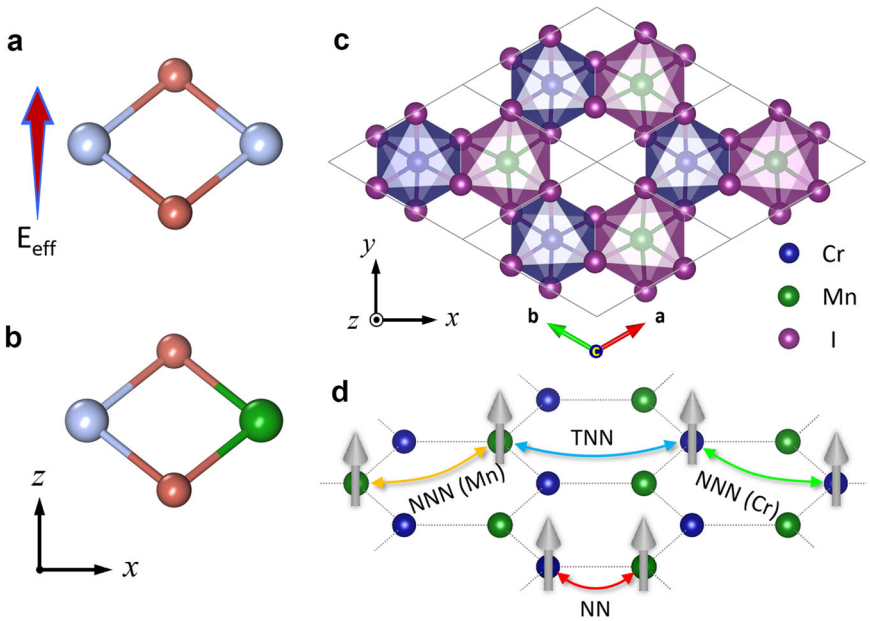

Fig. 1 Inversion symmetry breaking schemes and geometric structure. a, **b** Schematics of two different approaches to induce DMIs in monolayer magnets (silver/green balls: magnetic cations, orange balls: nonmagnetic anions). **a** The prevailing strategy, relying on an effective vertical electric field $\mathbf{E}_{eff}$. **b** Our strategy, by creating an asymmetric bipartite lattice. (**c**) Top view of the atomic structure of monolayer $CrMnI_6$, showing the Cr and Mn ions centered in edge-sharing CrI_6/MnI_6 octahedra. **d** The honeycomb spin lattice with the exchange couplings indicated.

implemented to 2D magnets, relies on breaking of the out-of-plane inversion symmetry via applying external electric field[17], or building Janus structures[18–20] or heterojunctions[21]. Whereas the strategy sketched in Fig. 1b, which breaks the in-plane inversion symmetry via involving two magnetic species, has not yet been exploited in 2D magnets and is the starting point of the present study. As a concrete example, Fig. 1c shows a $CrMnI_6$ monolayer which can be obtained by substituting one sublattice of chromium in the CrI_3 monolayer with manganese, and the ordered structure with bipartite spin lattice ($3\mu_B/Cr^{3+}$ and $4\mu_B/Mn^{3+}$ respectively) as shown in Fig. 1d is energetically favored[22]. This intriguing 2D magnet composed of binary magnetic elements has been predicted as a magnetic topological insulator exhibiting the quantum anomalous Hall effect[22]. Beyond the nontrivial electronic band topology, the system may possess more direct and intriguing nontrivial magnetic properties in real space. Indeed, the structural symmetry is reduced from D_{3d} to D_3 upon substitution. Because of the concurrence of centro-asymmetry and large spin-orbit coupling, the system is expected to harbor pronounced DMI and potentially more exotic anisotropic couplings like the case of well-studied Kitaev magnets[23].

To investigate the anisotropy of exchange couplings in the monolayer $CrMnI_6$ system, we first assume an atomistic spin Hamiltonian with bilinear (BL) terms,

$$H_{BL} = -\sum_i A_{i,zz} S_{iz}^2 - \sum_{i<j} \mathbf{S}_i \mathbf{J}_{ij}^{sym} \mathbf{S}_j - \sum_{i<j} \mathbf{D}_{ij} \cdot (\mathbf{S}_i \times \mathbf{S}_j) - \mu_B \sum_i \mathbf{B} \cdot \mathbf{S}_i. \quad (1)$$

The first term represents the single-ion anisotropy, which is reduced to a single scalar due to the three-fold rotational symmetry of the system. The second and third terms correspond to the symmetric and antisymmetric (DMI) parts of the pairwise exchange couplings, respectively, covering the nearest neighbor (NN), next NN (NNN) and third NN (TNN) pairs as exemplified in Fig. 1d. The last term accounts for the Zeeman energy.

We perform density functional theory calculation with a mean-field onsite Coulomb repulsion correction for the localized *d*-orbitals (DFT+U), to attain the energetics of the monolayer $CrMnI_6$ (see Methods section for details). For the magnetic degrees of freedom, we consider four specifically designed non-collinear spin configurations following the powerful four-state method[24–26], from which the exchange parameters can be conveniently extracted with DFT accuracy[15,24,27,28]. The calculated bilinear exchange parameters are summarized in Table 1. One can see that the symmetric exchange couplings are predominantly ferromagnetic, but exhibit highly anisotropic characteristics, as reflected by the distinctly different diagonal values in the $\mathbf{J}^{sym}$ tensors and some non-vanishing off-diagonal components. For the antisymmetric part (DMI), more insights can be drawn regarding both directions and magnitudes. For directions, our calculated DM vectors are consistent with the Moriya's rules[29], namely, the symmetry-forbidden components are numerically negligible as well (<0.01 meV). For magnitudes, the dominant NN $|\mathbf{D}|S_1S_2 = 0.63$ meV, is comparable to those in Cr (I, Br)$_3$ (0.61 meV) and Cr (I, Cl)$_3$ (0.43 meV)[19], but smaller than the magnitudes in Janus MnSeTe (2.14 meV) and MnSTe (2.63 meV)[30]. Practically, the $|\mathbf{D}|/J_{iso}$ ratio[31] is more widely used to evaluate the competition between the DMI and J_{iso}, which respectively favor canted and collinear alignments of the magnetic moments, with the trace average $J_{iso} = \mathrm{Tr}(\mathbf{J}^{sym})/3$. For the considered predominant bilinear exchange coupling strengths, the $|\mathbf{D}|/J_{iso}$ values reach 0.31 (NN Cr-Mn), 0.44 (Cr-Cr), and 0.82 (Mn-Mn) respectively. The first is comparable to the corresponding ratios in the prototypical Fe/Ir(111) system[32], while the latter two are much larger. Such pronounced chiral exchange couplings may enable topological magnetic excitations, when proper magnetocrystalline anisotropy and/or magnetic field are present.

Magnetocrystalline anisotropy and anisotropic biquadratic coupling

From the above discussions, another important physical aspect to investigate is the magnetocrystalline anisotropy energy (MAE), which indicates the easy magnetization orientations due to the interplay of multiple magnetic interactions. Our DFT+U calculations suggest that monolayer $CrMnI_6$ favors in-plane

magnetization, and the overall energy evolution trend can be qualitatively well reproduced by the bilinear model in Eq. (1) [Fig. 2a], indicating that the MAE partially stems from competition between bilinear interactions. On the other hand, there exists pronounced discrepancy at the quantitative level, which hints on the existence of some complex higher-order spin-spin interactions.

Given the protection of time-reversal symmetry[33], the likely leading higher-order term is the biquadratic (BQ) coupling[34–39]. To reveal the potential existence and microscopic origin of such BQ interactions, we systematically investigate the element-resolved single-ion and pair-resolved ion-ion contributions. The single-ion and NN exchange coupling are both found to be bilinear (See Supplementary Note 1 and Supplementary Figs. 1–2 for details). Then we study the NNN pairs by rotating the spins of one sublattice synchronically from x to z while fixing the other sublattice magnetized along y. Note that the NNN exchange couplings are in essence the NN Cr-Cr or Mn-Mn exchange couplings within the respective sublattices. This rotation operation is valid as long as more distant Cr-Cr or Mn-Mn interactions are much weaker. By comparing the energy evolutions between the DFT+U and BL model calculations, we see quantitative consistency upon rotating spins of the Cr sublattice. In stark contrast, pronounced differences exist when the spins of the Mn sublattice are rotated [Fig. 2b], strongly pointing to the likely source of the MAE discrepancy shown in Fig. 2a. Microscopically, this contrast could originate from their different 3*d*-electron fillings in the presence of an octahedral crystal field [Fig. 1c]. Both ions have three *d* electrons occupying the low-lying t_{2g} orbitals in the spin majority channel, while the Mn^{3+} ions (d^4) have an extra *d* electron populating the higher-energy e_g orbitals in the same spin channel. The exchange coupling of the e_g electrons within a Mn-Mn pair in return gives rise to pronounced BQ spin-spin interaction.

Table 1. Single-ion anisotropy and two-body exchange coupling strengths of the $CrMnI_6$ monolayer (unit: meV).

	J^{sym}	D
NN $Cr-Mn$ $(\mathbf{a}-\mathbf{b})/\sqrt{3}$	$\begin{bmatrix}1.15 & 0.00 & 0.00\\ 0.00 & 0.37 & 0.40\\ 0.00 & 0.40 & 0.51\end{bmatrix}$	$\begin{bmatrix}0.21\\ 0.00\\ 0.00\end{bmatrix}$
NNN $Cr-Cr$ $\mathbf{a}+\mathbf{b}$	$\begin{bmatrix}0.49 & 0.00 & 0.00\\ 0.00 & 0.44 & 0.06\\ 0.00 & 0.06 & 0.42\end{bmatrix}$	$\begin{bmatrix}0.00\\ 0.06\\ -0.19\end{bmatrix}$
NNN $Mn-Mn$ $\mathbf{a}+\mathbf{b}$	$\begin{bmatrix}-0.12 & 0.00 & 0.00\\ 0.00 & 0.93 & -0.28\\ 0.00 & -0.28 & 0.24\end{bmatrix}$	$\begin{bmatrix}0.00\\ -0.27\\ 0.10\end{bmatrix}$
TNN $Cr-Mn$ $\mathbf{b}-\mathbf{a}$	$\begin{bmatrix}0.19 & 0.00 & 0.00\\ 0.00 & 0.14 & 0.09\\ 0.00 & 0.09 & 0.22\end{bmatrix}$	$\begin{bmatrix}-0.03\\ 0.00\\ 0.00\end{bmatrix}$
A_{zz}(Cr)	0.28	
A_{zz}(Mn)	0.32	
MAE	DFT+U	2.05
$E_z - E_x$	BL	1.16
(meV/site)	BL+BQ	1.97

Note that the exchange couplings shown here are for specific pairs whose bond directions are indicated by the lattice vectors, with the tensor/vector components expressed in the global *xyz* coordinates as shown in Fig. 1c. Strengths of other pairs can be derived by symmetric transformation. The last three rows present the MAE calculated by using DFT+U method, as well as the BL and BL+BQ spin Hamiltonians, respectively.

We can now further improve the spin Hamiltonian in Eq. (1) on solid physics basis. Unlike earlier studied systems with isotropic BQ exchange couplings[35–39], one distinctive feature of the present 2D system is that the BQ coupling must be highly anisotropic, because it contributes substantially to the MAE (It therefore should also differ from the recently reported chiral biquadratic interaction[40], which is anisotropic but has zero contribution to MAE). Here, taking analogy to the simplest way of introducing exchange anisotropy in the bilinear regime[37], and borrowing the wisdom of deriving XXZ-type effective spin-spin interactions[41,42], we adopt a physically intuitive anisotropic form of BQ coupling,

$$H_{BQ} = -\frac{1}{2}\sum_{\langle i,j\rangle}^{i,j\in \mathrm{Mn}} \left(K_{\perp}S_{ix}S_{jx} + K_{\perp}S_{iy}S_{jy} + K_{\parallel}S_{iz}S_{jz}\right)^2, \quad (2)$$

with $K_{\perp}$ and $K_{\parallel}$ being the coefficients to be determined. With the inclusion of this BQ coupling, the energy evolution trend upon rotating the Mn sublattice spins can be significantly improved, as shown in Fig. 2b. As a crucial crosscheck, it also improves the description of the MAE quantitatively, as confirmed in Fig. 2a. The optimally compromised values of $K_{\perp}$ and $K_{\parallel}$ that can simultaneously improve the quantitative accuracies in both Fig. 2a and b is 0.2 and 0.1 $meV^{1/2}$ respectively, constituting a BQ contribution to easy-in-plane magnetization. The BQ coefficient seems to be weak at the first glance, but given the large magnetic moments of

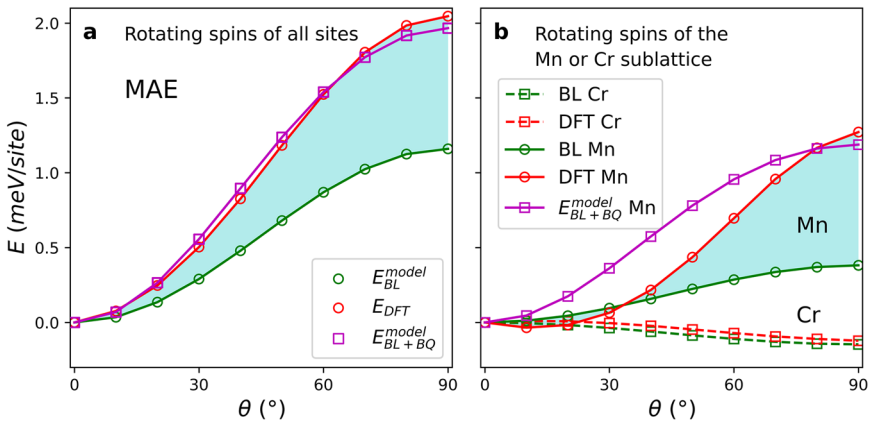

Fig. 2 Magnetic anisotropy. a Energy evolution of the FM configuration with rotating magnetization axis. **b** Energy evolution upon rotating spins of the Mn (Cr) sublattice from x ($\theta = 0°$) to z ($\theta = 90°$) synchronically while fixing spins of the Cr (Mn) sublattice along y. The energy differences between the DFT+U calculations and Eq. (1) are shaded in cyan.

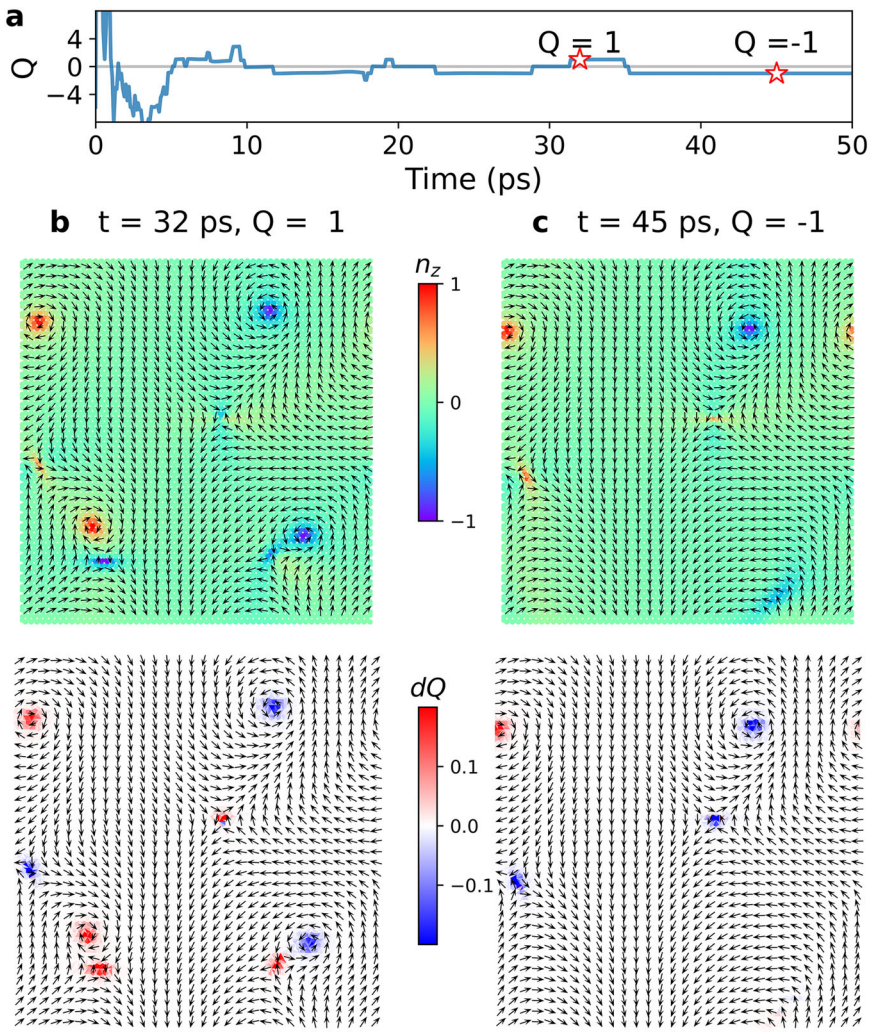

Fig. 3 Meronic excitations. a Evolution of the topological charge in an LLG simulation starting from a randomly magnetized configuration. **b**, **c** Snapshot configurations (top row) and topological charge distributions (bottom row).

Mn (S = 2), the BL [$J_{iso}S^2 = 1.4$ meV] and BQ [$K_{\perp}^2 S^4 = 0.64$ meV] coupling strengths between NN Mn-Mn pairs are readily comparable. Note that the well-studied isotropic BQ coupling has been recognized to play an important role in the magnetic ground state, spin dynamics and fluctuation of layered magnetic systems[35–39], and proved crucial in realizing the famous topological Haldane phase[34]. Here our work amounts to a concrete example of material hosting anisotropic high-order exchange couplings with pronounced strength, which also opens a new door to exploit unknown intricate exchange couplings via element mutation.

Bimeronic topological excitations and BKT-like transition

The BL-BQ spin Hamiltonian combining Eqs. (1) and (2) now provides an accurate description of the bipartite spin lattice of monolayer $CrMnI_6$. The giant D/J ratios point to possible vortex excitations with spin chirality in the system (Supplementary Note 2 and Supplementary Fig. 3). To explore potential topological excitations, we carry out atomistic magnetics simulations by numerically integrating the Landau–Lifshitz–Gilbert (LLG) equation[43], to model a fast cooling process from the paramagnetic state, and calculate the topological charge Q[44] to trace the dynamic evolution of real-space geometric phase. As shown in Fig. 3a, Q fluctuates drastically during the initial transient period of the simulation, and then converges to lower values, indicating the emergence of topological chiral spin textures upon cooling. Furthermore, the snapshots in Fig. 3b, c clearly show the existence of vortex- or antivortex-like local excitations. Given that the material strongly favors in-plane magnetization, we assign these nontrivial magnetic structures to merons instead of skyrmions that require out-of-plane magnetization[45]. Specifically, we may have merons (Q = −1/2) and anti-merons (Q = 1/2), as well as their various paired forms (including bimerons with Q = −1, anti-bimerons with Q = 1, and meron plus anti-meron pairs with Q = 0). We also note that the integer pairing of two meronic excitations involving one vortex plus one antivortex, fulfills the generic vorticity conservation condition, which is analogous to the topological defects of a 2D system below the critical temperature of the Berezinskii–Kosterlitz–Thouless transition[3–5]. Such nontrivial chiral magnetic structures are observed in several independent simulations with different initial states and/or damping parameters, further confirming their intrinsic nature.

The DMI-enabled abundant nano-sized bimeronic excitations and the easy in-plane magnetization strongly enhanced by the BQ coupling are indicative of magnetic transition beyond Landau's paradigm. To gain further insights into the magnetic critical behavior, we simulate the dynamics of the spin lattice under varying temperatures, with the thermal effect modeled by a stochastic magnetic fields scaled with temperature. To resolve the

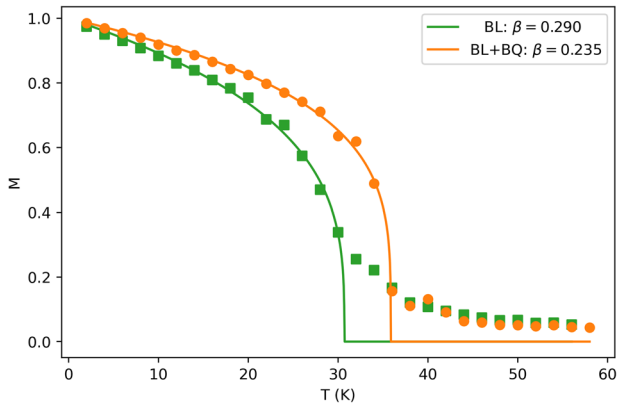

Fig. 4 Critical behavior. Magnetic critical behavior of monolayer $CrMnI_6$ simulated in the absence or presence of the identified anisotropic BQ coupling. The data points are from spin dynamics simulations while the curves are exponential fittings by using $M(T) = M(0)(1 - T/T_C)^{\beta}$.

effect of the BQ coupling, simulations without and with the term described by Eq. (2) are performed separately. The results are summarized and exponentially fitted in Fig. 4, showing that the pronounced BQ coupling not only enhances the transition temperature of the system from ~30.7 K to ~35.1 K, but also alters the exponent depicting the critical behavior, β, from 0.290 to 0.235. The out-of-plane cores of the merons also exhibit shrinking size when the BQ coupling is included (Supplementary Fig. 4). Note that in the paradigmatic 2D XY model elucidating the Berezinskii–Kosterlitz–Thouless transition[3–5], $\beta = 3\pi^2/128 \sim 0.231$[46]. Here in monolayer $CrMnI_6$, the in-plane and out-of-plane components of the Mn-Mn BQ coupling are both strong but anisotropic. Their uncompensated contribution enhances the easy-plane nature and renders the system a promising platform to exploit magnetic Berezinskii–Kosterlitz–Thouless physics with a critical temperature higher than the recently reported monolayer $CrCl_3$[47].

DISCUSSION

Our work demonstrates the existence of biquadratic exchange couplings with distinctive anisotropic form in the bipartite $CrMnI_6$ monolayer, and shows its essential influence on the low-energy excitation and critical behavior of the spin lattice. With these insights, it would be interesting to revisit existing magnetic materials for identifying potentially sizable anisotropic biquadratic exchange interactions, especially for those simultaneously harboring high-spin state and strong spin-orbit coupling. The former is universally required for biquadratic or even higher-order exchange interactions, while the latter is essential for inducing anisotropy. Contrasting the Cr and Mn sublattices of $CrMnI_6$ in terms of the negligible and pronounced anisotropic biquadratic exchange couplings, it is natural to perceive that band-filling is also an important factor. The anisotropic biquadratic exchange coupling is expected to play an important role in predicting magnetic properties and interpreting experimental results when its energy scale is comparable with the anisotropy from the bilinear order (both single-ion and pairwise contribution), or even overwhelms the latter. Relevant phenomena for manifestation include the magnetic ground state, magnetocrystalline anisotropy, low-energy excitations, either collective (e.g. magnons) or solitonic (e.g. skyrmions or merons), and magnetic critical behavior of magnetic materials. On the theoretical side, it is convenient to contrast these properties with and without involving the anisotropic biquadratic term to quantify its influence, while on the experimental side, hints on its existence might arise from failure of interpreting some observations based solely on the bilinear spin model.

Summarizing, we have systematically investigated the single-ion, pairwise exchange, and magnetocrystalline anisotropy of monolayer $CrMnI_6$, a recently predicted 2D magnet featured by in-plane inversion symmetry breaking that is distinctly different from the parental CrI_3 and its existing Janus derivatives. The bipartite spin lattice of $CrMnI_6$ enables coexistence of giant DMI and strong XXZ-type biquadratic coupling within the Mn sublattice with high-spin state. The interplay of anisotropic microscopic couplings gives rise to strongly preferred in-plane magnetization, facilitating the system to harbor nanometric bimeronic excitations and exhibit Berezinskii–Kosterlitz–Thouless-like critical behavior. Collectively, these central findings characterize $CrMnI_6$ as an emergent versatile member in the family of 2D magnets for realizing intriguing topological magnetism and critical phenomena. The present study may also stimulate further interests in more in-plane inversion asymmetric 2D magnets containing multiple magnetic species and hosting unexplored anisotropic magnetic properties, given the recent progress in controllable growth of such compounds[48].

METHODS

Ab initio calculations

We perform first-principles calculations to determine the spin exchange interactions in $CrMnI_6$ monolayer implementing the Vienna Ab initio Simulation Package (VASP)[49]. The projector augmented wave method[50,51] is used and the energy cutoff for plane waves to expand the valence electron wave functions is 350 eV. The gradient-corrected functional parameterized by Perdew, Burke and Ernzerhof (PBE)[52] is adopted to treat the electron exchange-correlation. A Γ-centered k-mesh is used to sample the Brillouin zone, with a grid density of $9 \times 9 \times 1$, $4 \times 4 \times 1$, and $2 \times 2 \times 1$ for unit cell, 2×2, and 3×3 supercell respectively. Denser k-grids have been tested to ensure the convergence of calculated total energy and derived exchange parameters. A constrained magnetic field is imposed to guide the electronic state converging to the designated spin configurations[53]. A high accuracy energy convergence threshold of 10^{-7} eV/cell is implemented in the self-consistent calculations. To account for the strong onsite Coulomb repulsion of the d shell electrons of Cr and Mn ions, the rotationally invariant DFT+U scheme proposed by Dudarev et al.[54] is implemented, with the effective U values being 2 and 4 eV respectively. A detailed discussion surrounding the influence of effective U values on the studied magnetic properties is presented in Supplementary Note 3 and Supplementary Figure 5. Visualization of crystal structure is enabled by VESTA[55].

The parameterization of the bilinear spin model in Eq. (1) is accomplished by using the four-state method[24–26]. This method can delicately cancel out interactions with irrelevant spins and has been widely implemented for mapping the ab initio total energy to an effective spin Hamiltonian. The single-ion anisotropy and NN exchange couplings are calculated within the 2×2 supercell, while the NNN and TNN exchange couplings are calculated using the 3×3 supercell.

In our calculations, we constrain the orientations of the atomic magnetic moments to specific directions following the four-state method, and relax their magnitudes to converge the charge density to the constrained local minimum. We inspect the results from two aspects to warrant that the constrained-magnetism calculations have converged to the desired state. (1) The local magnetic moments obtained from the constrain-magnetism calculations have same amplitude as those of the unconstrained collinear case (3 and 4 μ_B for Cr^{3+} and Mn^{3+} respectively); (2) the penalty energy due to the constraint has been minimized to less

than 0.02 meV by properly choosing the Lagrangian multiplier λ[53]. Specifically, for the $CrMnI_6$ monolayer studied in the present work, our extensive testing calculations suggest that $\lambda = 2$ works very well in achieving convergence of both magnetic moments and penalty energy.

Atomistic LLG simulations

To explore potential chiral magnetic structures and their dynamics, we numerically integrate the LLG equation[43]

$$\frac{d\mathbf{n}_i}{dt} = -\frac{\gamma}{(1+\alpha^2)\mu_i}[\mathbf{n}_i \times \mathbf{B}_i^{\text{eff}} + \alpha \mathbf{n}_i \times (\mathbf{n}_i \times \mathbf{B}_i^{\text{eff}})]. \quad (3)$$

Here the subscript i indexes the spin sites; the first and second terms on the right-hand side represent respectively the precession and damping of the normalized local spin $\mathbf{n}_i$; γ is the electron gyromagnetic ratio, and α is the Gilbert damping parameter for which we take the value of 0.3 in our simulations. The local effective field $\mathbf{B}_i^{\text{eff}} = -\partial H/\partial \mathbf{n}_i$ originates from both the intrinsic exchange couplings and external magnetic field.

We numerically integrate the LLG equation [Eq. (3)] with time to model the dynamics of localized spins formed by Cr + Mn honeycomb lattice. To tackle with the complex spin interaction as described by combining Eqs. (1) and (2), we have developed an in-house code[56] based on Python and parallelized by message passing interface (MPI). The time step is set to $\delta t = 1$ fs and the Depondt modified Heun's method[57] is implemented for numerical integration so that the magnitudes of spins conserve throughout the simulations. Periodic boundary condition is applied in all simulations. The temporal effect is modeled by adding a thermal field to the local effective exchange field in Eq. (3), which scales with the temperature[58]

$$\mathbf{B}_i^{th} = \sqrt{\frac{2\alpha k_B \mu_i}{\gamma \delta t}} \boldsymbol{\eta}_i(T) \quad (4)$$

Here $\boldsymbol{\eta}_i(T)$ is the white noise for spin site i, which obeys the normal random distribution and is updated for each time step; k_B is the Boltzmann constant, T is the temperature in K, and other quantities follow Eq. (3). This modulation converts the LLG equation from deterministic to stochastic in the spirit of Langevin dynamics[59].

In the atomistic LLG simulations, the spin lattice is modeled by a normalized vector field, namely, each classic spin is treated as a unit vector. The bipartite characteristic of the studied $CrMnI_6$ monolayer is captured by the following technical treatments. (1) When calculating the effective exchange field $\mathbf{B}_i^{\text{exch}}$, the single-ion anisotropy and bilinear exchange couplings are separately considered for the two sublattices to distinguish Cr and Mn, and the BQ-type exchange only exists in the Mn-sublattice following the first-principle results. The spin quantum numbers (S=3/2 for Cr and S=2 for Mn) are absorbed into the single-ion anisotropy and exchange-coupling parameters. (2) When calculating the torque induced by the external Zeeman fields $\mathbf{B}_i^{\text{ext}}$ (including the stochastic field mimicking the thermal effect), the local moments of 3 and $4\mu_B$ are multiplied for Cr^{3+} and Mn^{3+} respectively.

Calculation of topological charges

The topological charge Q depicts the evolution of geometric phase of chiral magnetic structures. In micromagnetic systems where the magnetization $\mathbf{n}(\mathbf{r})$ and its spatial gradients are continuous, the topological charge can be calculated by mapping the 2D spatial magnetization to the surface of a sphere[13]

$$Q = \frac{1}{4\pi}\int_S \mathbf{n}(\mathbf{r}) \cdot [\partial_x \mathbf{n}(\mathbf{r}) \times \partial_y \mathbf{n}(\mathbf{r})] d\mathbf{r}. \quad (5)$$

In atomic magnetic lattices with discrete spin sites, Q is calculated by using the scheme proposed by Berg and Lüscher[44],

$$Q = \frac{1}{4\pi}\sum_l A_l, \quad (6)$$

with

$$\cos\left(\frac{A_l}{2}\right) = \frac{1 + \mathbf{n}_i \cdot \mathbf{n}_j + \mathbf{n}_j \cdot \mathbf{n}_k + \mathbf{n}_k \cdot \mathbf{n}_i}{2(1 + \mathbf{n}_i \cdot \mathbf{n}_j)(1 + \mathbf{n}_j \cdot \mathbf{n}_k)(1 + \mathbf{n}_k \cdot \mathbf{n}_i)} \quad (7)$$

where i, j, and k are indices of sites on a triangular plaquette from the Delaunay triangulation of the spin lattice, and A_l is the solid angle measuring the relative canting of the three spins (See ref. [60] for detailed sketch).

DATA AVAILABILITY

The data that support the findings of this study are included in this article and are available from the corresponding author upon reasonable request.

CODE AVAILABILITY

The simulation codes required for obtaining the results presented in this paper are available on reasonable request to the corresponding author.

Received: 24 February 2023; Accepted: 30 June 2023;
Published online: 26 July 2023

REFERENCES

1. Mermin, N. D. & Wagner, H. Absence of ferromagnetism or antiferromagnetism in one- or two-dimensional isotropic Heisenberg models. *Phys. Rev. Lett.* **17**, 1133–1136 (1966).
2. Hohenberg, P. C. Existence of long-range order in one and two dimensions. *Phys. Rev.* **158**, 383–386 (1967).
3. Berezinsky, V. L. Destruction of long range order in one-dimensional and two-dimensional systems having a continuous symmetry group. I. Classical systems. *Sov. Phys. JETP* **32**, 493–500 (1971).
4. Berezinsky, V. L. Destruction of Long-range order in one-dimensional and two-dimensional systems possessing a continuous symmetry group. II. Quantum systems. *Sov. Phys. JETP* **34**, 610 (1972).
5. Kosterlitz, J. M. & Thouless, D. J. Long range order and metastability in two dimensional solids and superfluids. (application of dislocation theory). *J. Phys. C: Solid State Phys.* **5**, L124–L126 (1972).
6. Huang, B. et al. Layer-dependent ferromagnetism in a van der Waals crystal down to the monolayer limit. *Nature* **546**, 270–273 (2017).
7. Gong, C. et al. Discovery of intrinsic ferromagnetism in two-dimensional van der Waals crystals. *Nature* **546**, 265–269 (2017).
8. Dzyaloshinsky, I. A thermodynamic theory of "weak" ferromagnetism of antiferromagnetics. *J. Phys. Chem. Solids* **4**, 241–255 (1958).
9. Moriya, T. New mechanism of anisotropic superexchange interaction. *Phys. Rev. Lett.* **4**, 228–230 (1960).
10. Parkin, S. & Yang, S.-H. Memory on the racetrack. *Nat. Nanotechnol.* **10**, 195–198 (2015).
11. Mühlbauer, S. et al. Skyrmion lattice in a chiral magnet. *Science* **323**, 915–919 (2009).
12. Yu, X. Z. et al. Real-space observation of a two-dimensional skyrmion crystal. *Nature* **465**, 901–904 (2010).
13. Tokura, Y. & Kanazawa, N. Magnetic skyrmion materials. *Chem. Rev.* **121**, 2857 (2021).
14. Yu, X. Z. et al. Transformation between meron and skyrmion topological spin textures in a chiral magnet. *Nature* **564**, 95–98 (2018).
15. Xu, C., Feng, J., Xiang, H. & Bellaiche, L. Interplay between Kitaev interaction and single ion anisotropy in ferromagnetic CrI_3 and $CrGeTe_3$ monolayers. *npj Comput. Mater.* **4**, 57 (2018).
16. Zhu, F. et al. Topological magnon insulators in two-dimensional van der waals ferromagnets $CrSiTe_3$ and $CrGeTe_3$: Toward intrinsic gap-tunability. *Sci. Adv.* **7**, eabi7532 (2021).
17. Liu, J., Shi, M., Lu, J. & Anantram, M. P. Analysis of electrical-field-dependent Dzyaloshinskii-Moriya interaction and magnetocrystalline anisotropy in a two-dimensional ferromagnetic monolayer. *Phys. Rev. B* **97**, 054416 (2018).

18. Cui, Q., Liang, J., Shao, Z., Cui, P. & Yang, H. Strain-tunable ferromagnetism and chiral spin textures in two-dimensional Janus chromium dichalcogenides. *Phys. Rev. B* **102**, 094425 (2020).
19. Xu, C. et al. Topological spin texture in Janus monolayers of the chromium trihalides Cr(I, X)$_3$. *Phys. Rev. B* **101**, 060404 (2020).
20. Yuan, J. et al. Intrinsic skyrmions in monolayer Janus magnets. *Phys. Rev. B* **101**, 094420 (2020).
21. Sun, W. et al. Controlling bimerons as skyrmion analogues by ferroelectric polarization in 2D van der Waals multiferroic heterostructures. *Nat. Commun.* **11**, 5930 (2020).
22. Zhang, H., Yang, W., Cui, P., Xu, X. & Zhang, Z. Prediction of monolayered ferromagnetic $CrMnI_6$ as an intrinsic high-temperature quantum anomalous Hall system. *Phys. Rev. B* **102**, 115413 (2020).
23. Lee, J.-H. et al. Multiple spin-orbit excitons in α-$RuCl_3$ from bulk to atomically thin layers. *npj Quantum Mater.* **6**, 43 (2021).
24. Xiang, H., Kan, E., Wei, S.-H., Whangbo, M. H. & Gong, X. Predicting the spin-lattice order of frustrated systems from first principles. *Phys. Rev. B* **84**, 224429 (2011).
25. Xiang, H., Lee, C., Koo, H.-J., Gong, X. & Whangbo, M.-H. Magnetic properties and energy-mapping analysis. *Dalton. Trans.* **42**, 823–853 (2013).
26. Šabani, D., Bacaksiz, C. & Milošević, M. V. Ab initio methodology for magnetic exchange parameters: generic four-state energy mapping onto a Heisenberg spin Hamiltonian. *Phys. Rev. B* **102**, 014457 (2020).
27. Xu, C. et al. Possible Kitaev quantum spin liquid state in 2D materials with S=3/2. *Phys. Rev. Lett.* **124**, 087205 (2020).
28. Xu, C. et al. Electric-field switching of magnetic topological charge in Type-I multiferroics. *Phys. Rev. Lett.* **125**, 037203 (2020).
29. Moriya, T. Anisotropic superexchange interaction and weak ferromagnetism. *Phys. Rev.* **120**, 91–98 (1960).
30. Liang, J. et al. Very large Dzyaloshinskii-Moriya interaction in two-dimensional Janus manganese dichalcogenides and its application to realize skyrmion states. *Phys. Rev. B* **101**, 184401 (2020).
31. Fert, A., Cros, V. & Sampaio, J. Skyrmions on the track. *Nat. Nanotechnol.* **8**, 152–156 (2013).
32. Heinze, S. et al. Spontaneous atomic-scale magnetic skyrmion lattice in two dimensions. *Nat. Phys.* **7**, 713–718 (2011).
33. Brinker, S., dos Santos Dias, M. & Lounis, S. Prospecting chiral multisite interactions in prototypical magnetic systems. *Phys. Rev. Res.* **2**, 033240 (2020).
34. Mila, F. & Zhang, F.-C. On the origin of biquadratic exchange in spin 1 chains. *Eur. Phys. J. B* **16**, 7–10 (2000).
35. Wysocki, A. L., Belashchenko, K. D. & Antropov, V. P. Consistent model of magnetism in ferropnictides. *Nat. Phys.* **7**, 485–489 (2011).
36. Zhu, H.-F. et al. Giant biquadratic interaction-induced magnetic anisotropy in the iron-based superconductor $A_xFe_{2-y}Se_2$. *Phys. Rev. B* **93**, 024511 (2016).
37. Kartsev, A., Augustin, M., Evans, R. F. L., Novoselov, K. S. & Santos, E. J. G. Biquadratic exchange interactions in two-dimensional magnets. *npj Comput. Mater.* **6**, 150 (2020).
38. Paul, S., Haldar, S., von Malottki, S. & Heinze, S. Role of higher-order exchange interactions for skyrmion stability. *Nat. Commun.* **11**, 4756 (2020).
39. Ni, J. et al. Giant biquadratic exchange in 2D magnets and its role in stabilizing ferromagnetism of $NiCl_2$ monolayers. *Phys. Rev. Lett.* **127**, 247204 (2021).
40. Brinker, S., dos Santos Dias, M. & Lounis, S. The chiral biquadratic pair interaction. *N. J. Phys.* **21**, 083015 (2019).
41. Rachel, S. & Le Hur, K. Topological insulators and Mott physics from the Hubbard interaction. *Phys. Rev. B* **82**, 075106 (2010).
42. Vaezi, A., Mashkoori, M. & Hosseini, M. Phase diagram of the strongly correlated Kane-Mele-Hubbard model. *Phys. Rev. B* **85**, 195126 (2012).
43. Gilbert, T. L. A phenomenological theory of damping in ferromagnetic materials. *IEEE Trans. Magn.* **40**, 3443–3449 (2004).
44. Berg, B. & Lüscher, M. Definition and statistical distributions of a topological number in the lattice O(3) σ-model. *Nucl. Phys. B* **190**, 412–424 (1981).
45. Göbel, B., Mertig, I. & Tretiakov, O. A. Beyond skyrmions: review and perspectives of alternative magnetic quasiparticles. *Phys. Rep.* **895**, 1–28 (2021).
46. Bramwell, S. T. & Holdsworth, P. C. W. Magnetization and universal sub-critical behaviour in two-dimensional XY magnets. *J. Phys. Condens. Matter* **5**, L53 (1993).
47. Bedoya-Pinto, A. et al. Intrinsic 2D-XY ferromagnetism in a van der Waals monolayer. *Science* **374**, 616–620 (2021).
48. Zhou, J. et al. Composition and phase engineering of metal chalcogenides and phosphorous chalcogenides. *Nat. Mater.* **22**, 450–458 (2023).
49. Kresse, G. & Furthmüller, J. Efficient iterative schemes for ab initio total-energy calculations using a plane-wave basis set. *Phys. Rev. B* **54**, 11169–11186 (1996).
50. Blöchl, P. E. Projector augmented-wave method. *Phys. Rev. B* **50**, 17953–17979 (1994).
51. Kresse, G. & Joubert, D. From ultrasoft pseudopotentials to the projector augmented-wave method. *Phys. Rev. B* **59**, 1758–1775 (1999).
52. Perdew, J. P., Burke, K. & Ernzerhof, M. Generalized gradient approximation made simple. *Phys. Rev. Lett.* **77**, 3865–3868 (1996).
53. Ma, P.-W. & Dudarev, S. L. Constrained density functional for noncollinear magnetism. *Phys. Rev. B* **91**, 054420 (2015).
54. Dudarev, S. L., Botton, G. A., Savrasov, S. Y., Humphreys, C. J. & Sutton, A. P. Electron-energy-loss spectra and the structural stability of nickel oxide: An LSDA +U study. *Phys. Rev. B* **57**, 1505–1509 (1998).
55. Momma, K. & Izumi, F. VESTA 3 for three-dimensional visualization of crystal, volumetric and morphology data. *J. Appl. Crystallogr.* **44**, 1272–1276 (2011).
56. Zhang, S. PyASD: python-based atomistic spin dynamics and Monte Carlo simulators. https://pypi.org/project/pyasd (2023) .
57. Depondt, P. & Mertens, F. G. Spin dynamics simulations of two-dimensional clusters with Heisenberg and dipole-dipole interactions. *J. Phys. Condens. Matter* **21**, 336005 (2009).
58. Lee, K. J., Park, N. Y. & Lee, T. D. Numerical study of spin relaxation by thermal fluctuation: effect of shape anisotropy. *J. Appl. Phys.* **89**, 7460–7462 (2001).
59. Chubykalo, O., Hannay, J. D., Wongsam, M., Chantrell, R. W. & Gonzalez, J. M. Langevin dynamic simulation of spin waves in a micromagnetic model. *Phys. Rev. B* **65**, 184428 (2002).
60. Müller, G. P. et al. Spirit: multifunctional framework for atomistic spin simulations. *Phys. Rev. B* **99**, 224414 (2019).

ACKNOWLEDGEMENTS

S.Z. acknowledges Dr. C. S. Xu for kind help in the four-state method related calculations. This work was supported by the National Natural Science Foundation of China (Grant Nos. 11904350, 11634011, 11974323, 11722435, and 12274276), the Innovation Program for Quantum Science and Technology (Grant No. 2021ZD0302800), the Strategic Priority Research Program of Chinese Academy of Sciences (Grant No. XDB30000000), the Anhui Initiative in Quantum Information Technologies (Grant No. AHY170000), and Anhui Provincial Natural Science Foundation (Grant. No. 2008085QA30).

AUTHOR CONTRIBUTIONS

Z.Z. conceived the idea and directed the project. S.Z. and X.L. performed ab initio calculations with valuable input from H.Z., and developed codes for atomistic LLG simulations. All authors analyzed and discussed the results, and wrote the manuscript. S.Z. and X.L. contributed equally to this work.

COMPETING INTERESTS

The authors declare no competing interests.

ADDITIONAL INFORMATION

Supplementary information The online version contains supplementary material available at https://doi.org/10.1038/s41535-023-00569-4.

Correspondence and requests for materials should be addressed to Zhenyu Zhang.

Reprints and permission information is available at http://www.nature.com/reprints

Publisher's note Springer Nature remains neutral with regard to jurisdictional claims in published maps and institutional affiliations.